Research Article Vol. 32, No. 12 / 3 Jun 2024 / Optics Express 21755
Optics EXPRESS

Fast simulation for interacting four-level Rydberg atoms: electromagnetically induced transparency and Autler-Townes splitting

XINYI Y. I. XU,[1] GUODA XIE,[2] JINLOU MA,[3] LEI YING,[3] JINPENG YUAN,[4] ZHIXIANG HUANG,[2] AND WEI E. I. SHA[1,*]

[1]College of Information Science Electronic Engineering, Zhejiang University, Hangzhou 310027, China
[2]Key Laboratory of Intelligent Computing and Signal Processing, Ministry of Education, Anhui University, Hefei 230039, China
[3]School of Physics, Zhejiang University, Hangzhou 310027, China
[4]State Key Laboratory of Quantum Optics and Quantum Optics Devices, Institute of Laser Spectroscopy, Shanxi University, Taiyuan 030006, China
[*]weisha@zju.edu.cn

Abstract: Quantum sensing using Rydberg atoms is an emerging technology for precise measurement of electric fields. However, most existing computational methods are all based on a single-particle model and neglect Rydberg-Rydberg interaction between atoms. In this study, we introduce the interaction term into the conventional four-level optical Bloch equations. By incorporating fast iterations and solving for the steady-state solution efficiently, we avoid the computation of a massive $4^N \times 4^N$ dimensional matrix. Additionally, we apply the Doppler frequency shift to each atom used in the calculation, eliminating the requirement for an additional Doppler iteration. These schemes allow for the calculation of the interaction between 7000 atoms around one minute. Based on the many-body model, we investigate the Rydberg-Rydberg interaction of Rydberg atoms under different atomic densities. Furthermore, we compare our results with the literature data of a three-level system and the experimental results of our own four-level system. The results demonstrate the validity of our model, with an effective error of 4.59% compared to the experimental data. Finally, we discover that the many-body model better predicts the linear range for measuring electric fields than the single-particle model, making it highly applicable in precise electric field measurements.

© 2024 Optica Publishing Group under the terms of the Optica Open Access Publishing Agreement

1. Introduction

Based on Rydberg atoms, quantum sensing technology has attracted interest of researchers in recent years, and experienced extensive development [1–7]. Due to their large polarizability and concentration of transition frequencies in the microwave range, Rydberg atoms are extremely sensitive to externally applied microwave fields [8–10], enabling precise measurement of electric fields [3]. In comparison to traditional antennas, Rydberg atoms offer the following advantages [11–14]:

1. Encompassing a broad frequency spectrum from DC to terahertz range, due to the richness of Rydberg atomic energy levels.
2. Providing independent measurements of microwave fields, irrespective of prevailing technologies.
3. Minimizing interference during measurements due to the absence of metallic components in the detector.
4. Establishing a correlation between microwave field measurements and fundamental physical constants, such as Planck's constant and optical frequency measurements.

#523897 https://doi.org/10.1364/OE.523897
Journal © 2024 Received 19 Mar 2024; revised 11 May 2024; accepted 23 May 2024; published 30 May 2024

Optics EXPRESS

5. Facilitating automatic demodulation in communication applications.

These advantages make Rydberg atoms widely applicable in the fields of quantum sensing, quantum imaging, and atomic communication receivers [15].

However, relevant theoretical studies only focus on a four-level model based on a single-particle approximation, ignoring the Rydberg-Rydberg interaction between atoms [1–7]. The complex Rydberg-Rydberg [16,17] interaction between atoms make investigating these interaction extremely challenging. Researchers have previously modeled the interaction in three-level systems and obtained simulation results using the reduced density matrix expansion method and Monte Carlo rate equation (MCRE) approach [18–21]. However, these methods inevitably suffer from the complexities of theoretical modeling and the significant time required for computer simulation. If applied to the four-level system, these issues would become even more severe.

In this work, using the existing theories on many-body effects in three-level systems, we propose a fast simulation method that replaces transient solutions of optical Bloch equations with steady-state solutions. By implementing fast linear iterations to avoid matrix operations in higher dimensions, we achieve good agreement between our proposed method and MCRE approach in literature, with even better performance in some cases than the MCRE approach [18]. Based on the three-level system model, we also present a many-body model for a four-level system considering the Rydberg-Rydberg interaction between Rydberg atoms. In addition to the aforementioned fast iterative technique, we incorporate the Doppler frequency shift into each atom, eliminating the need for an additional Doppler iteration and achieving convergence within a few steps. Through numerical experiments, we first observe that the many-body effect becomes significant as the density of atomic vapor increases. Then, we compare our simulation results with laboratory experiments and find that our many-body model better matches the actual phenomenon of the right peak decrease in electromagnetically induced transparency (EIT) [14] and Autler-Townes (AT) splitting [22,23]. Finally, we provide an analysis of the linear range of the electric field for both the single-particle model and the many-body model.

2. Four-level many-body interaction model

We consider a four-level system with a ladder-type energy level structure, as shown in Fig. 1(a). Initially, the atoms are all in the ground state of the first energy level. By using a probe laser, the atoms are excited from the ground state to the second energy level. Simultaneously, a second coupling laser is employed to excite the atoms from the second energy level to the third energy level (Rydberg state), which is a highly excited state. Due to the presence of the coupling laser, a destructive quantum interference phenomenon occurs, resulting in a transparent window for atomic absorption of the probe laser, thereby increasing the atomic vapor's transmittance to the probe laser. This phenomenon is known as EIT. At this stage, if a microwave field is coupled, the Rydberg atoms in the third energy level can be excited to neighboring Rydberg states, namely the fourth energy level. This leads to a decrease in transmittance of the probe laser and the splitting of the original EIT peak, known as the AT splitting.

However, in practical situations, van der Waals forces induced by the Rydberg-Rydberg interaction also exist between the excited Rydberg atoms, and this interaction force is inversely proportional to the sixth power of the distance R^6, as shown in Fig. 1(b). As a result, atoms that are closer together exert a much larger force on each other, and this force rapidly decays with interaction distance. Therefore, in cases where the atomic vapor density is higher, this interaction force becomes increasingly significant and cannot be ignored.

In the presence of interatomic interaction forces, the traditional optical Bloch equations are modified as follows:

$$\frac{\partial \rho^{(i)}}{\partial t} = -\frac{\mathrm{i}}{\hbar}[H_0 + U^{(i)}, \rho^{(i)}] + L \tag{1}$$

Optics EXPRESS

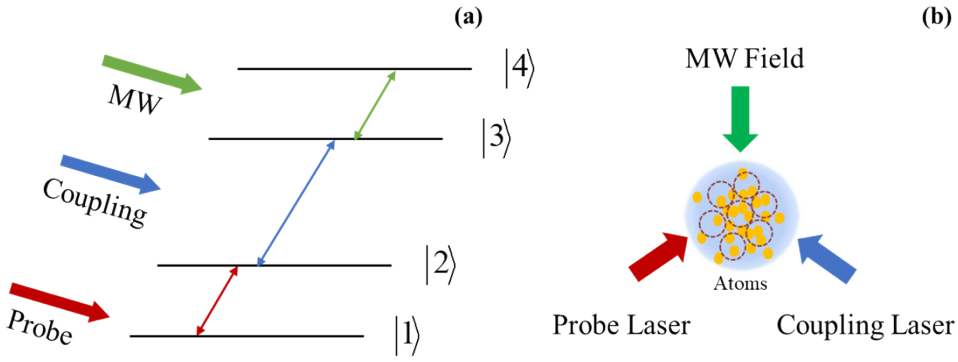

Fig. 1. (a) represents a diagram of the ladder-type energy levels, while (b) illustrates the schematic of the quantum sensing using Rydberg atoms.

where $\rho^{(i)}$ represents the density matrix of the atom i, H_0 denotes the Hamiltonian for independent atoms, and $U^{(i)}$ represents the interatomic interaction term that arises from other atoms, which can be found in Ref. [18]. And the interaction term $U^{(i)}$ is given by:

$$U^{(i)} = -C_6 \sum_{j \neq i} \frac{P_{rr}^{(i)} P_{rr}^{(j)}}{R_{ij}^6} \tag{2}$$

where $P_{rr}^{(i)} = |r_{ii} r|$ is the projector onto the Rydberg state of the atom i; R_{ij} is the distance between atom the i and atom j and C_6 is a constant [18,20].

Additionally, L represents the Lindblad operator and has the following expression:

$$L = \begin{bmatrix} \Gamma_2\rho_{22} & -\gamma_{12}\rho_{12} & -\gamma_{13}\rho_{13} & -\gamma_{14}\rho_{14} \\ -\gamma_{21}\rho_{21} & \Gamma_3\rho_{33} - \Gamma_2\rho_{22} & -\gamma_{23}\rho_{23} & -\gamma_{24}\rho_{24} \\ -\gamma_{31}\rho_{31} & -\gamma_{32}\rho_{32} & \Gamma_4\rho_{44} - \Gamma_3\rho_{33} & -\gamma_{34}\rho_{34} \\ -\gamma_{41}\rho_{41} & -\gamma_{42}\rho_{42} & -\gamma_{43}\rho_{43} & -\Gamma_4\rho_{44} \end{bmatrix} \tag{3}$$

In this model, $\gamma_{ij} = \frac{\Gamma_i + \Gamma_i}{2}$ and $\Gamma_{i,j}$ represent the transition decay rates. The model does not include collision and dephasing terms. Although atomic collisions, Penning ionization, and ion electric fields can theoretically cause dephasing, these effects can be mitigated by reducing vapor pressure, decreasing beam intensity, and limiting the interaction time between atoms and the field [3].

The expression for H_0 is as follows:

$$H_0 = \frac{\hbar}{2} \begin{bmatrix} 0 & \Omega_p & 0 & 0 \\ \Omega_p & -2\Delta_p & \Omega_c & 0 \\ 0 & \Omega_c & -2(\Delta_p + \Delta_c) & \Omega_{mw} \\ 0 & 0 & \Omega_{mw} & -2(\Delta_p + \Delta_c + \Delta_{mw}) \end{bmatrix} \tag{4}$$

where Ω_p, Ω_c, and Ω_{mw} represent the Rabi frequencies of the probe laser, coupling laser, and microwave field, respectively, while Δ_p, Δ_c, and Δ_{mw} correspond to the frequency detunings for

Optics EXPRESS

these three external driven fields. The detuning term is defined as:

$$\Delta_i = \omega_i - \omega_{i0},\ i = p, c, mw \tag{5}$$

where ω_i represents the angular frequencies of the probe laser, coupling laser, and microwave field, while ω_{i0} represents the resonant angular frequencies between neighboring energy levels.

By solving the aforementioned equation, we obtain:

$$\begin{aligned}
\dot{\rho}_{11}^{(i)} &= \mathrm{i}\frac{\Omega_p}{2}(\rho_{12}^{(i)} - \rho_{21}^{(i)}) + \Gamma_2\rho_{22}^{(i)} \\
\dot{\rho}_{21}^{(i)} &= [\mathrm{i}\Delta_p - \gamma_{21}]\rho_{21}^{(i)} + \mathrm{i}\frac{\Omega_p}{2}(\rho_{22}^{(i)} - \rho_{11}^{(i)}) - \mathrm{i}\frac{\Omega_c}{2}\rho_{31}^{(i)} \\
\dot{\rho}_{22}^{(i)} &= -\mathrm{i}\frac{\Omega_p}{2}(\rho_{12}^{(i)} - \rho_{21}^{(i)}) + \mathrm{i}\frac{\Omega_c}{2}(\rho_{23}^{(i)} - \rho_{32}^{(i)}) - \Gamma_2\rho_{22}^{(i)} + \Gamma_3\rho_{33}^{(i)} \\
\dot{\rho}_{31}^{(i)} &= [\mathrm{i}(\Delta_p + \Delta_c) - \gamma_{31}]\rho_{31}^{(i)} + \mathrm{i}\frac{\Omega_p}{2}\rho_{32}^{(i)} - \mathrm{i}\frac{\Omega_c}{2}\rho_{21}^{(i)} - \mathrm{i}\frac{\Omega_{mw}}{2}\rho_{41}^{(i)} \\
\dot{\rho}_{32}^{(i)} &= [\mathrm{i}\Delta_c - \gamma_{32}]\rho_{32}^{(i)} + \mathrm{i}\frac{\Omega_c}{2}(\rho_{33}^{(i)} - \rho_{22}^{(i)}) + \mathrm{i}\frac{\Omega_p}{2}\rho_{31}^{(i)} - \mathrm{i}\frac{\Omega_{mw}}{2}\rho_{42}^{(i)} \\
\dot{\rho}_{33}^{(i)} &= -\mathrm{i}\frac{\Omega_c}{2}(\rho_{23}^{(i)} - \rho_{32}^{(i)}) + \mathrm{i}\frac{\Omega_{mw}}{2}(\rho_{34}^{(i)} - \rho_{43}^{(i)}) - \Gamma_3\rho_{33}^{(i)} + \Gamma_4\rho_{44}^{(i)} \\
\dot{\rho}_{41}^{(i)} &= [\mathrm{i}(\Delta_p + \Delta_c + \Delta_{mw}) - \gamma_{41}]\rho_{41}^{(i)} + \mathrm{i}\frac{\Omega_p}{2}\rho_{42}^{(i)} - \mathrm{i}\frac{\Omega_{mw}}{2}\rho_{31}^{(i)} - \mathrm{i}\sum_{i\neq j} V_{ij}\dot{\rho}_{44}^{(j)}\rho_{41}^{(i)} \\
\dot{\rho}_{42}^{(i)} &= [\mathrm{i}(\Delta_c + \Delta_{mw}) - \gamma_{42}]\rho_{42}^{(i)} + \mathrm{i}\frac{\Omega_p}{2}\rho_{41}^{(i)} + \mathrm{i}\frac{\Omega_c}{2}\rho_{43}^{(i)} - \mathrm{i}\frac{\Omega_{mw}}{2}\rho_{32}^{(i)} - \mathrm{i}\sum_{i\neq j} V_{ij}\dot{\rho}_{44}^{(j)}\rho_{42}^{(i)} \\
\dot{\rho}_{43}^{(i)} &= [\mathrm{i}\Delta_{mw} - \gamma_{43}]\rho_{43}^{(i)} + \mathrm{i}\frac{\Omega_{mw}}{2}(\rho_{44}^{(i)} - \rho_{33}^{(i)}) + \mathrm{i}\frac{\Omega_c}{2}\rho_{42}^{(i)} - \mathrm{i}\sum_{i\neq j} V_{ij}\dot{\rho}_{44}^{(j)}\rho_{43}^{(i)} \\
\dot{\rho}_{44}^{(i)} &= -\mathrm{i}\frac{\Omega_{mw}}{2}(\rho_{34}^{(i)} - \rho_{43}^{(i)}) - \Gamma_4\rho_{44}^{(i)}
\end{aligned} \tag{6}$$

In this case, the density matrix ρ is a Hermitian matrix. By numerically solving the above equation, we can obtain the numerical solution to calculate the transmittance of atomic vapor, represented by ρ_{21}.

3. Iterative and steady-state solution

3.1. Iterative method

However, it is important to note that under the consideration of the interaction between atoms, the density matrix of each atom is influenced by other atoms, and the probability distribution of energy levels of the atom in question also affects other atoms. This relationship is mutually coupled, and an accurate solution requires a matrix operation of size $4^N \times 4^N$, where N is the number of atoms. Such matrix operations are computationally challenging for current computers, thus an iterative solution is considered.

For solving large-scale linear equation systems, Jacobi and Gauss-Seidel iteration methods are commonly employed [24,25]. These methods involve substituting the previous iteration's calculation results into the current step, thereby avoiding the computationally intensive inverse operation of large matrices. Similarly, our approach incorporates interatomic interaction terms obtained from the previous calculation into the solution of the density matrix in the current step. While this method may be hindered by slow convergence speeds and potential non-convergence issues [24], we have found that the statistical averaging effect of a large number of atoms enables

Optics EXPRESS

convergence to a desired error range with a reduced number of iteration steps.

$$\frac{\partial \rho^{(i)}\{k+1\}}{\partial t} = -\frac{\mathrm{i}}{\hbar}[H_0 + U^{(i)}\{k\}, \rho^{(i)}\{k+1\}] + L^{(i)}\{k+1\} \tag{7}$$

In the $k+1$ iteration, the interaction forces between atoms are calculated using the distribution of all atoms from the k-th iteration. This means that in each time iteration, only one differential equation with respect to t needs to be solved for each atom. Compared to inverting a matrix of size $4^N \times 4^N$, our iterative approach significantly reduces the computational workload.

3.2. Steady-state solution

For the differential equations of each atom in the above iterative method, we can employ the explicit and implicit Euler method or the Runge-Kutta method. The advantages of the iterative methods are that they do not need to handle complex formulae, and numerical implementation is relatively straightforward. However, the relatively high number of iterations reduces computational efficiency.

Considering the complexity of our system, we reconstruct the density matrices and derive corresponding steady-state solution. This method only requires one computation to obtain the values of all unknown density matrix elements, resulting in a higher computational efficiency.

The steady solution of the density matrix Eq. (7) can be expressed in matrix form as follows:

$$\frac{\partial \rho^{(i)}_{16\times1}\{\mathrm{n}+1\}}{\partial t} = [G]_{16\times16}\rho^{(i)}_{16\times1}\{\mathrm{n}+1\} \tag{8}$$

where ρ being expressed as:

$$\rho^{(i)}_{16\times1} = (\rho^{(i)}_{11}, \rho^{(i)}_{12}, \rho^{(i)}_{13}, \rho^{(i)}_{14}, \rho^{(i)}_{21}, \cdots, \rho^{(i)}_{44})^T \tag{9}$$

By applying the Kronecker product formula, we can obtain:

$$[G]\rho^{(i)}\{n+1\} = [(H_0 + U^{(j)}\{n\}) \otimes I - I \otimes (H_0 + U^{(j)}\{n\})^T + D]\rho^{(i)}\{n+1\} \tag{10}$$

where I is the identity matrix. To align with Eq. (8), the matrix L can be written in the following form:

$$L = D_{16\times16}\rho_{16\times1} \tag{11}$$

Optics EXPRESS

where D can be expressed as:

$$D = \begin{bmatrix}
0 & 0 & 0 & 0 & 0 & \Gamma_2 & 0 & 0 & 0 & 0 & 0 & 0 & 0 & 0 & 0 & 0 \\
0 & -\gamma_{12} & 0 & 0 & 0 & 0 & 0 & 0 & 0 & 0 & 0 & 0 & 0 & 0 & 0 & 0 \\
0 & 0 & -\gamma_{13} & 0 & 0 & 0 & 0 & 0 & 0 & 0 & 0 & 0 & 0 & 0 & 0 & 0 \\
0 & 0 & 0 & -\gamma_{14} & 0 & 0 & 0 & 0 & 0 & 0 & 0 & 0 & 0 & 0 & 0 & 0 \\
0 & 0 & 0 & 0 & -\gamma_{21} & 0 & 0 & 0 & 0 & 0 & 0 & 0 & 0 & 0 & 0 & 0 \\
0 & 0 & 0 & 0 & 0 & -\Gamma_2 & 0 & 0 & 0 & 0 & \Gamma_3 & 0 & 0 & 0 & 0 & 0 \\
0 & 0 & 0 & 0 & 0 & 0 & -\gamma_{23} & 0 & 0 & 0 & 0 & 0 & 0 & 0 & 0 & 0 \\
0 & 0 & 0 & 0 & 0 & 0 & 0 & -\gamma_{24} & 0 & 0 & 0 & 0 & 0 & 0 & 0 & 0 \\
0 & 0 & 0 & 0 & 0 & 0 & 0 & 0 & -\gamma_{31} & 0 & 0 & 0 & 0 & 0 & 0 & 0 \\
0 & 0 & 0 & 0 & 0 & 0 & 0 & 0 & 0 & -\gamma_{32} & 0 & 0 & 0 & 0 & 0 & 0 \\
0 & 0 & 0 & 0 & 0 & 0 & 0 & 0 & 0 & 0 & -\Gamma_3 & 0 & 0 & 0 & 0 & \Gamma_4 \\
0 & 0 & 0 & 0 & 0 & 0 & 0 & 0 & 0 & 0 & 0 & -\gamma_{34} & 0 & 0 & 0 & 0 \\
0 & 0 & 0 & 0 & 0 & 0 & 0 & 0 & 0 & 0 & 0 & 0 & -\gamma_{41} & 0 & 0 & 0 \\
0 & 0 & 0 & 0 & 0 & 0 & 0 & 0 & 0 & 0 & 0 & 0 & 0 & -\gamma_{42} & 0 & 0 \\
0 & 0 & 0 & 0 & 0 & 0 & 0 & 0 & 0 & 0 & 0 & 0 & 0 & 0 & -\gamma_{43} & 0 \\
0 & 0 & 0 & 0 & 0 & 0 & 0 & 0 & 0 & 0 & 0 & 0 & 0 & 0 & 0 & -\Gamma_4
\end{bmatrix} \tag{12}$$

When the system reaches a steady state, Eq. (8) can be expressed as follows:

$$[G]\rho^{(i)}\{n+1\} = 0 \tag{13}$$

However, it should be noted that the components of the density matrix are not entirely independent. This is because an atom exists in one of the four energy levels, leading to the following constraint equations:

$$\rho_{11}^{(i)}\{n+1\} + \rho_{22}^{(i)}\{n+1\} + \rho_{33}^{(i)}\{n+1\} + \rho_{44}^{(i)}\{n+1\} = 1 \tag{14}$$

By substituting (14) into (13), we obtain:

$$[G]\rho^{(i)}\{n+1\} = b \tag{15}$$

The density matrix can be obtained by directly solving the inverse of a low-dimensional matrix, greatly reducing computational time.

$$\rho^{(i)}\{n+1\} = [G]^{-1}b \tag{16}$$

4. Doppler effect in the iterative process

In a four-level system, without considering the Doppler effect, the EIT-AT spectrum used to measure the electric field intensity will become distorted [3]. However, the conventional approach in simulation models is to consider the Doppler frequency shift that each atom may experience at each frequency sampling of the probe laser, and then perform the Doppler averaging. This approach is not feasible in many-body models because each frequency sampling significantly increases the computational time. Therefore, in our fast algorithm, we consider to introduce the different Doppler frequency shift to each atom individually, and finally perform the Doppler averaging for all atoms at each frequency sampling. In this step, we effectively convert the statistical average of individual atoms into an ensemble average of the entire atomic system, thereby eliminating computational time significantly.

Optics EXPRESS

In the experiment, the probe laser and the coupling laser propagate in opposite directions, resulting in the following detunings:

$$\widetilde{\Delta}_p^{(i)} = \Delta_p^{(i)} - \frac{2\pi}{\lambda_p} v^{(i)} \quad \widetilde{\Delta}_c^{(i)} = \Delta_c^{(i)} + \frac{2\pi}{\lambda_c} v^{(i)} \tag{17}$$

where v represents the average velocity of atoms. The expression for Doppler averaging is as follows:

$$\rho_{21_D} = \frac{1}{\sqrt{\pi}u} \int_{-3u}^{3u} \rho_{21}^{(i)} \left(\widetilde{\Delta}_p^{(i)}, \widetilde{\Delta}_c^{(i)} \right) e^{\frac{-v^2}{u^2}} dv \tag{18}$$

Among them, $u = \sqrt{\frac{2k_B T}{m}}$, m represents the atomic mass, T denotes the temperature in Kelvin, and k_B stands for the Boltzmann constant. And Eq. (18) can be efficiently solved by using a simple trapezoidal rule of numerical integration due to the fast decay nature of the exponential function included.

5. Numerical results

5.1. Comparison of three-level systems

All the theories and formulae above are based on a four-level system, but they can be analogously applied to a three-level system. In Ref. [18], experiments were conducted on a many-body system of three-level Rydberg atoms, and the MCRE approach was used to model the many-body system. To validate our fast algorithm, we repeated the numerical experiments in literature using the same parameter settings. The atomic vapor density was $3.5 \times \frac{10^9}{cm^3}$, with 7000 atoms in the overlap volume of the laser. The frequencies of the probe laser were chosen as 2π×0.08 MHz in Fig. 2(a) and 2π×2.0 MHz in Fig. 2(b). The probe laser excites the Rydberg atoms from state $5S_{1/2}$ to state $5P_{3/2}$, with detuning ranging from -2π×20 MHz to 2π×20 MHz. The coupling laser, with a Rabi frequency of 2π×4.8 MHz, excites the Rydberg atoms from state $5P_{3/2}$ to state $60S_{1/2}$. Considering the lifetime of the Rydberg state $60S_{1/2}$ to be 100μs, this generates an effective dephasing rate of 10 kHz.

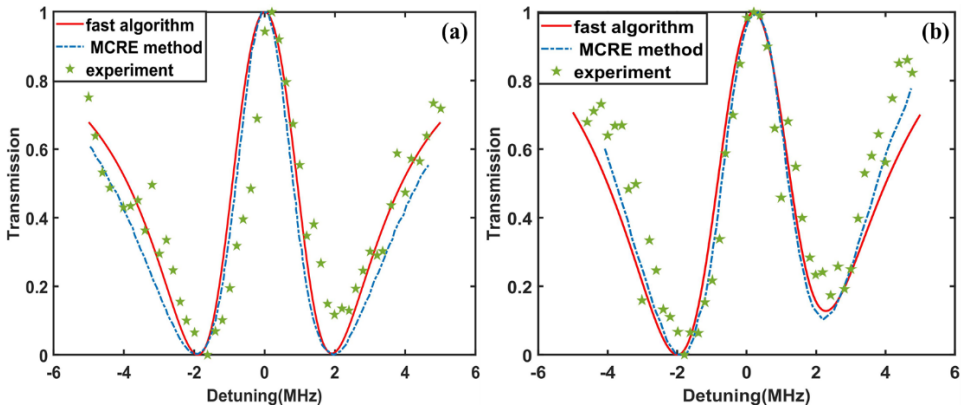

Fig. 2. The red solid line represents the data obtained from our fast algorithm, the blue dashed-dotted line represents the data calculated with the MCRE approach, and the green pentacles represent the actual measured data from the literature experiment. (a) corresponds to a probe laser Rabi frequency of 2π×0.08 MHz, while (b) corresponds to a probe laser Rabi frequency of $2\pi \times 2$ MHz.

In our modeling framework, the atoms are initially positioned at random coordinates within the glass chamber, which has a minor effect on the simulation outcomes. From a macroscopic

Optics EXPRESS

viewpoint, the approximately 7000 atoms are distributed uniformly throughout the chamber, yielding an averaged interaction calculation. At the microscopic level, the rarefied atomic vapor used in the experiment means that the number of atoms is relatively small compared to the chamber's size, making it unlikely for two atoms to be in extremely close proximity. Consequently, the possibility of two particles exhibiting extremely strong interactions is low, and the initial atomic positions have a minor impact on the simulation results.

From the experimental results, we can observe that in a three-level system, when the Rabi frequency of the probe laser is low, the heights of the two valleys are almost the same, indicating that the many-body effects are not significant. As the Rabi frequency of the probe laser increases, the right valley is elevated, indicating the presence of many-body effects. When the Rabi frequency of probe laser is $2\pi\times0.08$ MHz, the relative L2-norm error between our algorithm and the MCRE algorithm is 0.064; and when the Rabi frequency of probe laser is $2\pi\times2$ MHz, the corresponding error is 0.050. At the same time, when the Rabi frequency of probe laser is $2\pi\times0.08$ MHz, the error of the experimental results in the literature and the MCRE approach is 0.148, and the error between our algorithm and the experimental data in the literature is 0.104. Moreover, we comparatively studied the numerical performances between the traditional Runge-Kutta method [26] and our fast algorithm. The former required 6556.31 seconds to simulate 201 frequency points, whereas the latter took only 7.85 seconds, with a relative error of 0.82%. This significant difference in computational time demonstrates the superior efficiency of our method.

From above results, our algorithm successfully simulates both scenarios, showing good agreement with experimental data and the MCRE approach. And in certain cases, our fast algorithm outperforms the traditional MCRE approach and provides results that better fit the actual experimental data.

5.2. Comparison with different densities of four-level Rydberg atoms

The comparison with existing data on three-level many-body systems confirms the validity of our method to a certain extent. Next, we consider both the model and the data being restored to a four-level system to observe the relationship between the many-body effects and the density of Rydberg atomic vapors. Here, we set the Rabi frequencies of the probe laser and the coupling laser as $2\pi\times3$ MHz in Fig. 3(a) and $2\pi\times4$ MHz in Fig. 3(b), respectively. The microwave field

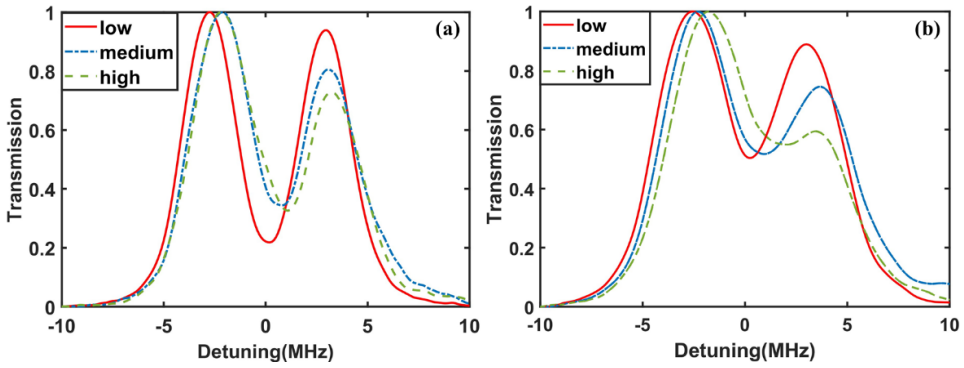

Fig. 3. The red solid line represents the atomic vapor density of $3.5\times\frac{10^9}{cm^3}$ (low), the blue dashed-dotted line represents a density of $8\times\frac{10^9}{cm^3}$ (medium), and the green dashed line represents a density of $1.2\times\frac{10^{10}}{cm^3}$ (high). (a) shows the Rabi frequencies of the probe laser and the coupling laser as $2\pi\times3$ MHz each, while (b) shows the Rabi frequencies as $2\pi\times4$ MHz each.

Optics EXPRESS

has a Rabi frequency of 2π×9.2 MHz. The densities of the atomic vapor are $3.5 \times \frac{10^9}{cm^3}$ (low), $8 \times \frac{10^9}{cm^3}$ (medium), and $1.2 \times \frac{10^{10}}{cm^3}$ (high). The EIT-AT spectra corresponding to the three densities are shown in Fig. 3.

By comparing to the classical EIT-AT spectra, we observe that considering the Rydberg-Rydberg interaction between atoms causes the two transmission peaks of the AT splitting to become asymmetric. Specifically, the peak on the right side of the symmetry axis is lower than the peak on the left side, and there is a certain degree of frequency shift. Additionally, these many-body effects become stronger as the density of the atomic vapor increases. This implies that ignoring the many-body effects can strongly impact the accuracy of numerical results, especially when the atomic gas density is high.

If we choose 201 points for frequency sampling and set an average L2-norm error of 0.01 as the convergence criterion of the steady solution, the computational time for modeling the interactions among 7,000 atoms is 81.52 seconds after three iterations.

5.3. Comparison with experimental data of four-level systems

In this section, we present the results of our experiments, which aim to demonstrate the accuracy of our many-body model. To specifically highlight the agreement between the many-body model results and experimental data in terms of asymmetry, we introduce a new indicator, called the asymmetry degree. We know that in a completely symmetrical graph, the function values of two points symmetrical about the axis of symmetry are identical, whereas the emergence of asymmetry induces a deviation in these values. Therefore, with respect to a specific axis of symmetry, we define the asymmetry degree δ of the entire graph as follows:

$$\delta = \sqrt{\sum_{i=1}^{n} \left(\frac{a_i - a_i{}'}{\bar{a}_i}\right)^2} \tag{19}$$

where a_i denotes the function value of a particular point in the symmetrical graph, a_i' represents the function value of its symmetrical counterpart, and $\bar{a}_i$represents the average of a_i and a_i'. Note that only half of the region demarcated by the axis of symmetry requires calculation. This indicator quantifies the asymmetry of the calculated graph, where δ=0 signifies perfect symmetry, and increasing δ values indicate greater asymmetry.

For the experiments, we used a probe wavelength of 780 nm, with a power of 19.35 μW and a beam diameter of 24 μm. The coupling laser has a wavelength of 480 nm, laser power of 438 mW, and a beam diameter of 372 μm. Additionally, the microwave frequency was set to 14.232 GHz corresponds to $53D_{5/2}$-$54P_{3/2}$ Rydberg transition, with an absolute power of -3 dBm W. The distance between the horn antenna aperture and the atomic gas chamber was 44 cm and density of the atomic vaper is $1.13 \times \frac{10^{10}}{cm^3}$. To validate our many-body model, we compared the experimental data with the calculations obtained using our fast algorithm, along with the data from the single-particle model. The comparisons are summarized in Fig. 4.

By considering the middle region of interest, the asymmetry degree of the single-particle model is 0, indicating perfect symmetry, while the asymmetry degree of the many-body model is 10.08, and that of the experimental results is 11.07. This suggests that our many-body model can effectively capture the asymmetry observed in the EIT-AT images of the experimental results. And the error rate of the single-particle model is calculated to be 6.65%, whereas the many-body model reduces it to 4.59%. This indicates improved accuracy, which is crucial for precise field measurements. It is worth mentioning that in the simulation, we set the convergence criterion to an average L2-norm error lower than 0.01, which ensures convergence of the fast algorithm after a minimal number of iterations, allowing for fast computation of the interatomic interaction terms.

Optics EXPRESS

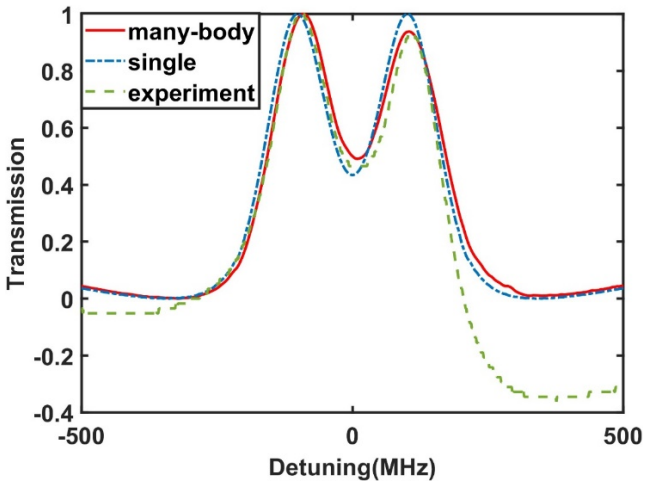

Fig. 4. The red solid line represents the simulated results from our fast algorithm for the many-body model, while the blue dashed-dotted line represents the results from the single-particle model. The green dashed line corresponds to the experimental data obtained.

In the situations with significant detuning, the experimental data may exhibit larger errors. This is due to the exchange-coupled mode of data collection, which filters out the DC component of the signal received by the photodetector. Operating at the device's optimal bias voltage, the photodetector minimizes signal fluctuations and enhances the acquired spectral signal. Consequently, the collected data display more pronounced signal changes at the onset and termination of the change. Notably, in EIT-AT split measurements, only the peak signal position is relevant, independent of the spectral positions at the beginning and end of the change. As a result, this phenomenon does not impact the analysis of our experimental results. If we choose the same points for frequency sampling and set the same convergence criterion of the steady solution, the computational time for modeling the interactions among 7,000 atoms is 91.73 seconds after three iterations.

5.4. Linear range of electric field measurement

In theory, the magnitude of the microwave field should be strictly proportional to the frequency interval between the two transmission peaks in the EIT-AT spectrum [3]. However, in practice, it is difficult to guarantee the linear relationship when the microwave field amplitude is small. Therefore, there exists a linear range for microwave field measurement, and the measured field amplitude should ideally be within this linear range. We set the Rabi frequencies of the probe laser and the coupling laser to both be $2\pi\times4$ MHz and both be $2\pi\times5$ MHz, respectively. By continuously changing the amplitude of the microwave field, we plot the linear range graphs for both the single-particle and many-body models, as shown in Fig. 5.

From the numerical results, it can be observed that the single-particle model exhibits a strict linear relationship at high-field amplitudes, and abruptly drops to zero at low amplitudes. This is inconsistent with reality, as there should be some fluctuations at high amplitudes and a buffering zone at low amplitudes. On the other hand, the many-body model can better meet these requirements, especially when the microwave field is weak. In such cases, the single-particle model may not provide accurate simulation, and therefore the many-body model should be adopted.

Optics EXPRESS

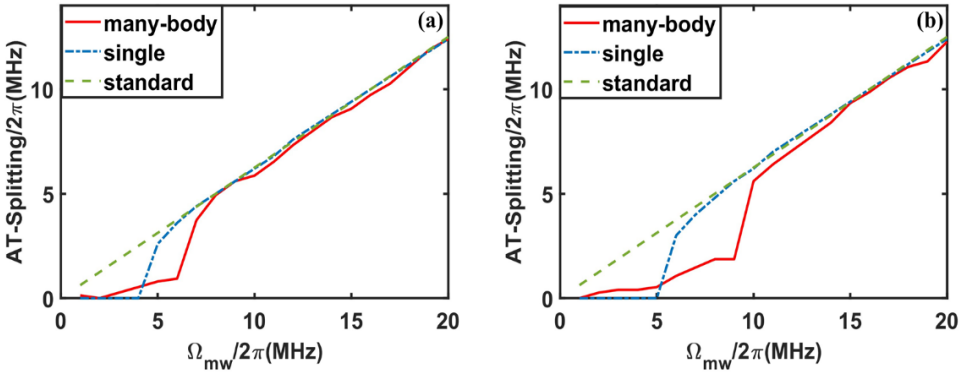

Fig. 5. The red solid line represents the simulation results of the many-body model using the fast algorithm, the blue dashed-dotted line represents the results of the single-particle model, and the green dashed line represents the theoretically strict linear relationship. (a) shows the Rabi frequencies of the probe laser and the coupling laser as $2\pi \times 4$ MHz and $2\pi \times 4$ MHz, respectively. (b) shows the Rabi frequencies of the probe laser and the coupling laser as $2\pi \times 5$ MHz and $2\pi \times 5$ MHz, respectively.

6. Conclusion

In conclusion, we first proposed a many-body model for a four-level system of Rydberg atoms. Building upon this model, we developed a fast linear iterative algorithm and a steady-state solution as a replacement for time-consuming transient solutions. Additionally, the Doppler frequency shift is incorporated into each atom for the many-body simulation. These schemes significantly reduced computational time and enhanced the operability of the many-body model. To validate the accuracy of our model, we degraded it to a three-level structure and compared it with existing literature data. Furthermore, we conducted corresponding simulations for the four-level system, and the comparative analyses demonstrated that our many-body model aligns well with experimental data. Subsequently, we performed relevant simulation to investigate the many-body effects for different atomic vapor densities and the linear range of electric field measurements. The results indicated the many-body model has a narrower linear range than the single-particle model, which is important for precise measurements of weak electric fields.

Funding. National Natural Science Foundation of China (61975177, U20A20164).

Disclosures. The authors declare that there are no conflicts of interest related to this article.

Data availability. Data underlying the results presented in this paper are not publicly available at this time but may be obtained from the authors upon reasonable request.

References

1. C. L. Holloway, M. T. Simons, J. A. Gordon, *et al.*, "Atom-Based RF Electric Field Metrology: From Self-Calibrated Measurements to Subwavelength and Near-Field Imaging," IEEE Trans. Electromagn. Compat. **59**(2), 717–728 (2017).
2. C. L. Holloway, J. A. Gordon, A. Schwarzkopf, *et al.*, "Broadband Rydberg Atom-Based Electric-Field Probe for SI-Traceable, Self-Calibrated Measurements," IEEE Trans. Antennas Propag. **62**(12), 6169–6182 (2014).
3. C. L. Holloway, M. T. Simons, J. A. Gordon, *et al.*, "Electric field metrology for SI traceability: Systematic measurement uncertainties in electromagnetically induced transparency in atomic vapor," J. Appl. Phys. **121**(23), 233106 (2017).
4. J. A. Sedlacek, A. Schwettmann, H. Kübler, *et al.*, "Atom-based vector microwave electrometry using rubidium Rydberg atoms in a vapor cell," Phys. Rev. Lett. **111**(6), 063001 (2013).
5. H. Fan, S. Kumar, J. Sedlacek, *et al.*, "Atom based RF electric field sensing," J. Phys. B: At. Mol. Opt. Phys. **48**(20), 202001 (2015).
6. J. A. Gordon, C. L. Holloway, A. Schwarzkopf, *et al.*, "Millimeter wave detection via Autler-Townes splitting in rubidium Rydberg atoms," Appl. Phys. Lett. **105**(2), 024104 (2014).

Optics EXPRESS

7. B. Liu, L. H. Zhang, Z. K. Liu, *et al.*, "Highly sensitive measurement of a megahertz rf electric field with a Rydberg-atom sensor," Phys. Rev. Appl. **18**(1), 014045 (2022).
8. B. Liu, L. Zhang, Z. Liu, *et al.*, "Electric field measurement and application based on Rydberg atoms," EMScience **1**(2), 1–16 (2023).
9. M. T. Simons, J. A. Gordon, C. L. Holloway, *et al.*, "Using frequency detuning to improve the sensitivity of electric field measurements via electromagnetically induced transparency and Autler-Townes splitting in Rydberg atoms," Appl. Phys. Lett. **108**(17), 174101 (2016).
10. J. Yuan, W. Yang, M. Jing, *et al.*, "Quantum sensing of microwave electric fields based on Rydberg atoms," Rep. Prog. Phys. **86**(10), 106001 (2023).
11. D. A. Anderson, R. E. Sapiro, and G. Raithel, "A self-calibrated SI-traceable Rydberg atom-based radio frequency electric field probe and measurement instrument," IEEE Trans. Antennas Propag. **69**(9), 5931–5941 (2021).
12. D. H. Meyer, Z. A. Castillo, K. C. Cox, *et al.*, "Assessment of Rydberg atoms for wideband electric field sensing," J. Phys. B: At. Mol. Opt. Phys. **53**(3), 034001 (2020).
13. C. T. Fancher, D. R. Scherer, M. C. S. John, *et al.*, "Rydberg atom electric field sensors for communications and sensing," IEEE Trans. Quantum Eng. **2**, 1–13 (2021).
14. J. M. Fleischhauer, A. Imamoglu, and J. P. Marangos, "Electromagnetically induced transparency: Optics in coherent media," Rev. Mod. Phys. **77**(2), 633–673 (2005).
15. C. L. Holloway, M. T. Simons, J. A. Gordon, *et al.*, "Detecting and receiving phase-modulated signals with a Rydberg atom-based receiver," IEEE Antennas Wirel. Propag. Lett. **18**(9), 1853–1857 (2019).
16. D. Møller, L. B. Madsen, and K. Mølmer, "Quantum gates and multiparticle entanglement by Rydberg excitation blockade and adiabatic passage," Phys. Rev. Lett. **100**(17), 170504 (2008).
17. M. Müller, I. Lesanovsky, H. Weimer, *et al.*, "Mesoscopic Rydberg gate based on electromagnetically induced transparency," Phys. Rev. Lett. **102**(17), 170502 (2009).
18. S. Sevincli, C. Ates, T. Pohl, *et al.*, "Quantum interference in interacting three-level Rydberg gases: coherent population trapping and electromagnetically induced transparency," J. Phys. B: At. Mol. Opt. Phys. **44**(18), 184018 (2011).
19. C. Ates, S. Sevincli, and T. Pohl, "Electromagnetically induced transparency in strongly interacting Rydberg gases," Phys. Rev. A **83**(4), 041802 (2011).
20. J. D. Pritchard, D. Maxwell, A. Gauguet, *et al.*, "Cooperative atom-light interaction in a blockaded Rydberg ensemble," Phys. Rev. Lett. **105**(19), 193603 (2010).
21. C. Ates, T. Pohl, T. Pattard, *et al.*, "Many-body theory of excitation dynamics in an ultracold Rydberg gas," Phys. Rev. A **76**(1), 013413 (2007).
22. N. B. Delone and V. P. Krainov, "AC Stark shift of atomic energy levels," Phys. Usp. **42**(7), 669–687 (1999).
23. J. S. Bakos, "AC stark effect and multiphoton processes in atoms," Phys. Rep. **31**(3), 209–235 (1977).
24. Y. Saad, *Iterative Methods for Sparse Linear Systems* (Society for Industrial and Applied Mathematics, 2003), Chap. 4.
25. G. H. Golub and C. F. Van Loan, *Matrix Computations* (JHU Press, 2013), Chap. 11.
26. F. B. Hildebrand, *Introduction to Numerical Analysis* (Courier Corporation, 1987), Chap. 6.

222.205.2.234 {ts '2024-06-20 05:15:31'}